

# Bottom-Up Synthesis of Graphene Monolayers with Tunable Crystallinity and Porosity

Christof Neumann,<sup>†</sup> David Kaiser,<sup>‡</sup> Michael J. Mohn,<sup>‡</sup> Matthias Füser,<sup>§</sup> Nils-Eike Weber,<sup>||</sup> Oliver Reimer,<sup>||</sup> Armin Götzhäuser,<sup>||</sup> Thomas Weimann,<sup>¶</sup> Andreas Terfort,<sup>\*,§,||</sup> Ute Kaiser,<sup>‡</sup> and Andrey Turchanin<sup>\*,†,‡,¶,⊥,||</sup>

<sup>†</sup>Institute of Physical Chemistry, Friedrich Schiller University Jena, 07743 Jena, Germany

<sup>‡</sup>Central Facility of Electron Microscopy, Ulm University, 89081 Ulm, Germany

<sup>§</sup>Institute of Inorganic and Analytical Chemistry, University of Frankfurt, 60348 Frankfurt, Germany

<sup>||</sup>Faculty of Physics, Bielefeld University, Bielefeld 33615, Germany

<sup>¶</sup>Physikalisch-Technische Bundesanstalt, 38116 Braunschweig, Germany

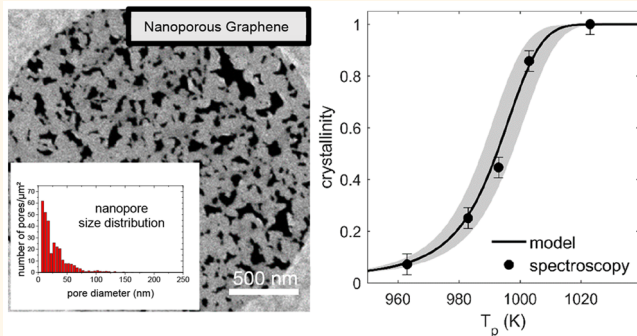
<sup>#</sup>Jena Center for Soft Matter (JCSM), 07743 Jena, Germany

<sup>⊥</sup>Center of Energy and Environmental Chemistry (CEEC Jena), 07743 Jena, Germany

## Supporting Information

**ABSTRACT:** We present a method for a bottom-up synthesis of atomically thin graphene sheets with tunable crystallinity and porosity using aromatic self-assembled monolayers (SAMs) as molecular precursors. To this end, we employ SAMs with pyridine and pyrrole constituents on polycrystalline copper foils and convert them initially into molecular nanosheets—carbon nanomembranes (CNMs)—via low-energy electron irradiation induced cross-linking and then into graphene monolayers via pyrolysis. As the nitrogen atoms are leaving the nanosheets during pyrolysis, nanopores are generated in the formed single-layer graphene. We elucidate the structural changes upon the cross-linking and pyrolysis down to the atomic scale by complementary spectroscopy and microscopy techniques including X-ray photoelectron and Raman spectroscopy, low energy electron diffraction, atomic force, helium ion, and high-resolution transmission electron microscopy, and electrical transport measurements. We demonstrate that the crystallinity and porosity of the formed graphene can be adjusted via the choice of molecular precursors and pyrolysis temperature, and we present a kinetic growth model quantitatively describing the conversion of molecular CNMs into graphene. The synthesized nanoporous graphene monolayers resemble a percolated network of graphene nanoribbons with a high charge carrier mobility ( $\sim 600 \text{ cm}^2/(\text{V s})$ ), making them attractive for implementations in electronic field-effect devices.

**KEYWORDS:** graphene, carbon nanomembranes, 2D phase transitions, nanopores, electric transport



Since the demonstration of isolated graphene sheets in 2004,<sup>1</sup> a variety of different two-dimensional (2D) materials have been discovered in the following years.<sup>2</sup> The synthesis of 2D materials with tunable structural, electrical, optical, and mechanical properties and their device integration is a prerequisite for their applications in nanotechnology and remains both a scientific and technological challenge.<sup>3</sup> Graphene monolayers, due to their extraordinary electronic properties such as low electronic noise in combination with high charge carrier mobility and atomic thickness, are attractive candidates for applications in nanobiotechnology, e.g., for sensing and ultrafiltration.<sup>4–7</sup> For these applications, graphene sheets have to be tailored to specific

properties. While sensing requires surface functionalization,<sup>8,9</sup> ultrafiltration requires the creation of nanopores, as pristine graphene monolayers are impermeable for atoms and molecules except for hydrogen ions.<sup>10</sup> To fabricate nanopores in graphene, typically focused ion beam milling with gallium or helium ions is employed.<sup>5,11</sup> Randomly distributed nanopores can be introduced into graphene by etching,<sup>12</sup> or they can be even intrinsically present in monolayers grown by chemical

Received: May 6, 2019

Accepted: May 21, 2019

vapor deposition (CVD).<sup>13</sup> However, these current approaches are very much limited in either their scalability or controllability. For chemical and biosensing with graphene-based field-effect transistors (FETs), specific functionalization has to be induced. As the covalent functionalization of the graphene plane results in defects and leads to a degradation of the electronic properties and a decrease in the sensitivity,<sup>14</sup> different approaches have been suggested to overcome this problem. These approaches include noncovalent functionalization of graphene FETs with complementary 2D materials<sup>8</sup> or implementation of graphene nanoribbons<sup>15</sup> or graphene nanomeshes<sup>16–18</sup> enabling functionalization of the edges. Thus, porous graphene sheets with high electronic quality and numerous edges available for the functionalization should significantly facilitate the sensor applications as well.

Here we present a scalable bottom-up synthesis of graphene monolayers with tunable crystallinity and porosity using nitrogen-containing (N-containing) aromatic self-assembled monolayers (SAMs) as molecular precursors on Cu(111) and technologically relevant polycrystalline copper foils. The developed route is presented in Figure 1. In the first growth step, Figure 1a (i), 4-(4-thiophenyl)pyridine (TPP) (b), 4-(1*H*-pyrrole-1-yl)thiophenol (PTP) (c), or 4-(2,5-dimethyl-1*H*-pyrrole-1-yl)thiophenol (DPTP) (d) compounds form a SAM on a copper substrate by vapor deposition (VD) under vacuum. In the second step, Figure 1a (ii), low-energy electron irradiation induced cross-linking converts the SAM into a molecular nanosheet: a carbon nanomembrane (CNM).<sup>19–21</sup> CNMs have been fabricated from different molecules,<sup>22</sup> and their structure and mechanical, optical, and electrical behavior can be engineered in this way.<sup>23–27</sup> The vacuum pyrolysis results in their conversion into graphene.<sup>23,28–30</sup> For the N-containing molecules (TPP, PTP, DPTP, Figure 1b) investigated in this study, we show that for a low pyrolysis temperature  $T_p^1$  nitrogen-doped nanocrystalline graphene is formed, Figure 1a (iii). By increasing the temperature to  $T_p^2$ , the recrystallization of the graphene sheet leads to the formation of nanopores by extrusion of the nitrogen atoms, Figure 1a (iv). We have found that the crystallinity and the porosity of the formed single-layer graphene sheets depends on the pyrolysis temperature. Moreover, there is a clear correlation between the structure of molecular compounds and density and size of the formed nanopores. We investigate this 2D transformation employing complementary spectroscopic and microscopic techniques including X-ray photoelectron spectroscopy (XPS), low-energy electron diffraction (LEED), Raman spectroscopy, helium ion microscopy (HIM), atomic force microscopy (AFM), aberration-corrected high-resolution transmission electron microscopy (HRTEM), and electrical transport measurements. The presence of various nitrogen–carbon bonds enables us to investigate the atomistic details of both the cross-linking process of SAMs into CNMs and the pyrolytic transformation of CNMs into graphene. We apply a modified Kolmogorov–Johnson–Mehl–Avrami (KJMA) model<sup>31</sup> to quantitatively describe the experimentally observed crystallinity of graphene as a function of pyrolysis temperature as well as the growth kinetics.

## RESULTS AND DISCUSSION

**Formation of N-Containing Aromatic SAMs.** First, we characterize the formation of TPP, PTP, and DPTP SAMs on Cu substrates (see Figure 1b–d for molecular structures) and their cross-linking into CNMs (steps i and ii in Figure 1a) by

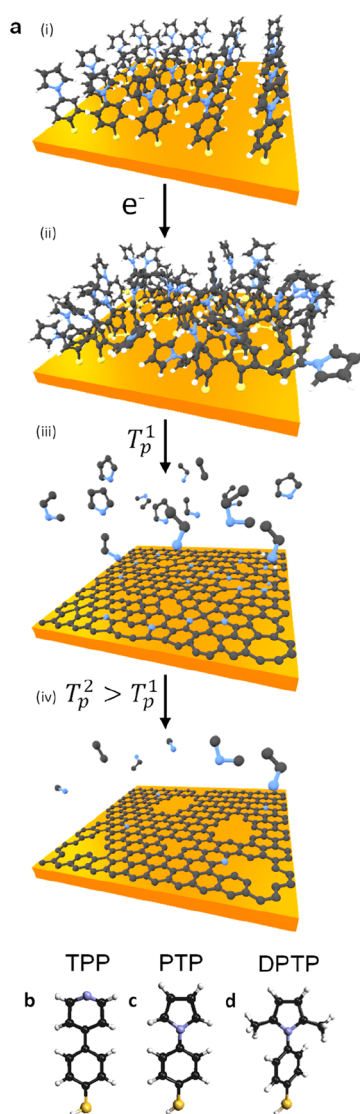


**Figure 1.** (a) Schematic representation of the growth of nanoporous graphene. The molecular compounds 4-(4-thiophenyl)pyridine (TPP, (b)), 4-(1*H*-pyrrole-1-yl)thiophenol (PTP, (c)), and 4-(2,5-dimethyl-1*H*-pyrrole-1-yl)thiophenol (DPTP, (d)) form self-assembled monolayers (SAMs) on Cu substrates by vapor deposition under vacuum (i). The SAMs are cross-linked *via* low-energy electron irradiation into molecular nanosheets, carbon nanomembranes (CNMs) (ii). Vacuum pyrolysis at a temperature  $T_p^1$  converts CNMs into nitrogen-doped nanocrystalline graphene (iii). By increasing the pyrolysis temperature to  $T_p^2$  nanopores are formed in the samples prepared from compounds (c) and (d).

XPS. We studied the formation of TPP SAMs and their subsequent transformations upon electron irradiation and pyrolysis on both single-crystalline Cu(111) and polycrystalline Cu foil substrates. As the obtained results are similar for both types of substrates, in the following PTP and DPTP SAMs were investigated only on the technologically relevant Cu foils. In Figure 2a the high-resolution XP spectra of TPP SAMs on Cu(111) for S 2p, C 1s, and N 1s core level electrons are shown; the respective data for TPP SAMs on Cu foils are presented in the Supporting Information (SI) Figure S1. No other XP signals with an exception of those for the metallic Cu substrate were detected. After the formation of the TPP SAM

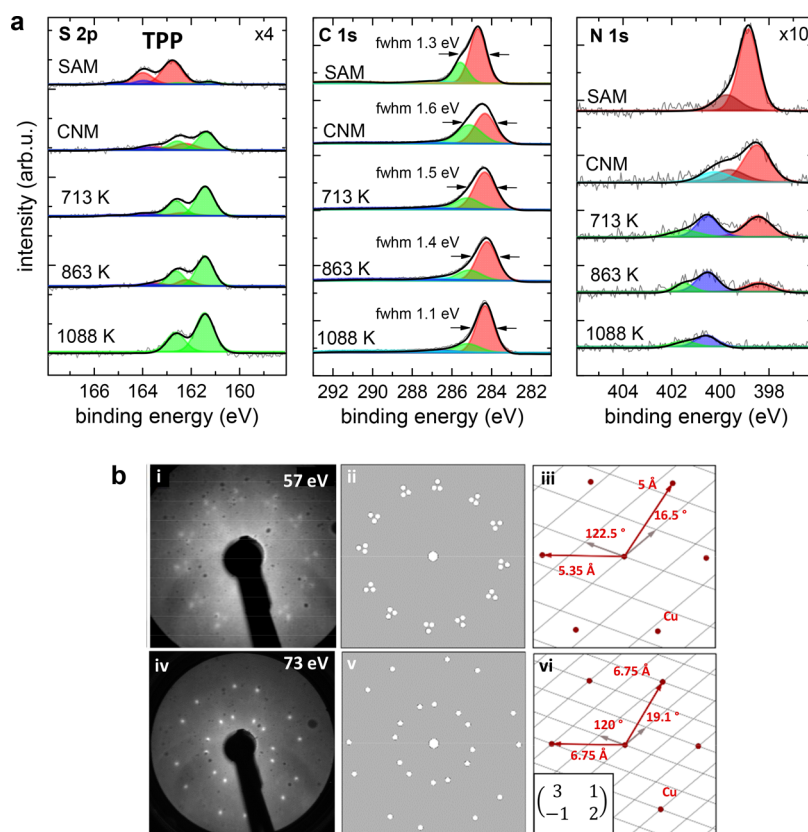


**Figure 2.** (a) X-ray photoelectron spectroscopy (XPS) of monolayers from the TPP compound on Cu(111). High-resolution S 2p, C 1s, and N 1s spectra during self-assembly, electron irradiation induced cross-linking, and pyrolysis at different temperatures. Intensities of the S 2p spectra and N 1s spectra are multiplied by a factor of 4 and 10, respectively. The spectral resolution is 0.9 eV. (b) Room-temperature (RT) experimental and simulated LEED patterns of TPP SAM on Cu(111) (i, ii) with the respective unit cell (iii). The RT data for the same sample after conversion into graphene at 1088 K (iv–vi).

by vacuum VD, the S 2p signal consists of a main doublet (red) due to the formation of thiulates with the binding energy (BE) of the S 2p<sub>3/2</sub> and S 2p<sub>1/2</sub> components at 162.6 and 163.8 eV,<sup>32</sup> respectively, contributing ~75% to the total S 2p intensity,  $I(\text{S } 2p)$ . Two other low-intensity sulfur species with BEs of S 2p<sub>3/2</sub> at 161.2 eV (green,  $I(\text{S } 2p) \approx 13\%$ ) and at 163.8 eV (blue,  $I(\text{S } 2p) \approx 12\%$ ) correspond to copper sulfides and disulfides. The formation of these species during vacuum VD of aromatic thiols on Cu can be attributed to a partial decomposition of the thiols in this process.<sup>29</sup> The C 1s signal of the formed TPP SAM consists of a main peak at 284.7 eV (red) with a full width at half-maximum (fwhm) of 1.0 eV, which is due to aromatic (sp<sup>2</sup>) C–C bonds and a second peak at 285.6 eV (fwhm = 0.9 eV) (green) due to the C–S and C=N bonds. Their intensity ratio of  $(8 \pm 1)/3$  fits well with the chemical composition. Furthermore, two low-intensity shakeup satellites at 288.0 eV (orange) and 291.6 eV (light blue) can be identified (see also Figure S1a). The N 1s signal has a main intensity at a BE of 398.8 eV, as expected for pyridine groups (red).<sup>33</sup> At a BE of 399.7 eV, an additional nitrogen species can be recognized (brown), which is most probably formed by the reaction of the pyridine groups with the hydrogen atoms released from the thiol groups during the self-assembly process.<sup>34,35</sup> From the attenuation of the substrate Cu 2p signal the effective thickness of the TPP SAMs is calculated to be ~9 Å, which indicates the formation of a densely packed SAM. This result is further confirmed by the LEED data presented in Figure 2b (i–iii). The observed diffraction

pattern, Figure 2b (i), represents an incommensurate structure of the TPP SAM on Cu(111) with an approximate unit cell characterized by vectors with lengths of 5.00 and 5.35 Å and an angle of 122.5°, Figure 2b (ii,iii), with a surface coverage of 22.6 Å<sup>2</sup> per molecule. This unit cell is rotated with respect to Cu(111) by an angle of 16.5°, forming 12 rotational domains. A similar structural arrangement was reported also for 1,1'-biphenyl-4-thiol (BPT) SAMs on Cu(111).<sup>29</sup>

Similar to the TPP SAMs, Figure 3 shows the S 2p, C 1s, and N 1s spectra of the PTP and DPTP SAMs on polycrystalline copper foils. The S 2p spectra are comparable to the TPP SAM, as the thiolate binding group is identical for all molecular compounds. The C 1s spectrum of the PTP SAM has a BE of 284.6 eV (fwhm 1.0 eV) (red) and is accompanied by a shoulder at 285.5 eV (green) (fwhm 1.4 eV) attributed to C–S bonds and the C=N bonds in the pyrrole group (Figure 3a). The C 1s spectrum of the DPTP SAM shows a similar behavior with the exception of a shoulder at 283.9 eV (magenta) due to additional methyl groups attached to the pyrrole ring which donate more electrons into the conjugated system (Figure 3b). In order to unambiguously confirm the presence of this shoulder, the C 1s spectrum of the DPTP SAM was analyzed by XPS with higher energy resolution (see Figure S2). The N 1s spectra of the PTP and DPTP SAM consist of a single species due to the pyrrole group but with slightly different BEs (PTP, Figure 3a, 400.7 eV, purple; DPTP, Figure 3b, 400.1 eV, turquoise), which correspond well to the literature values.<sup>33,36</sup> The origin of this difference is in



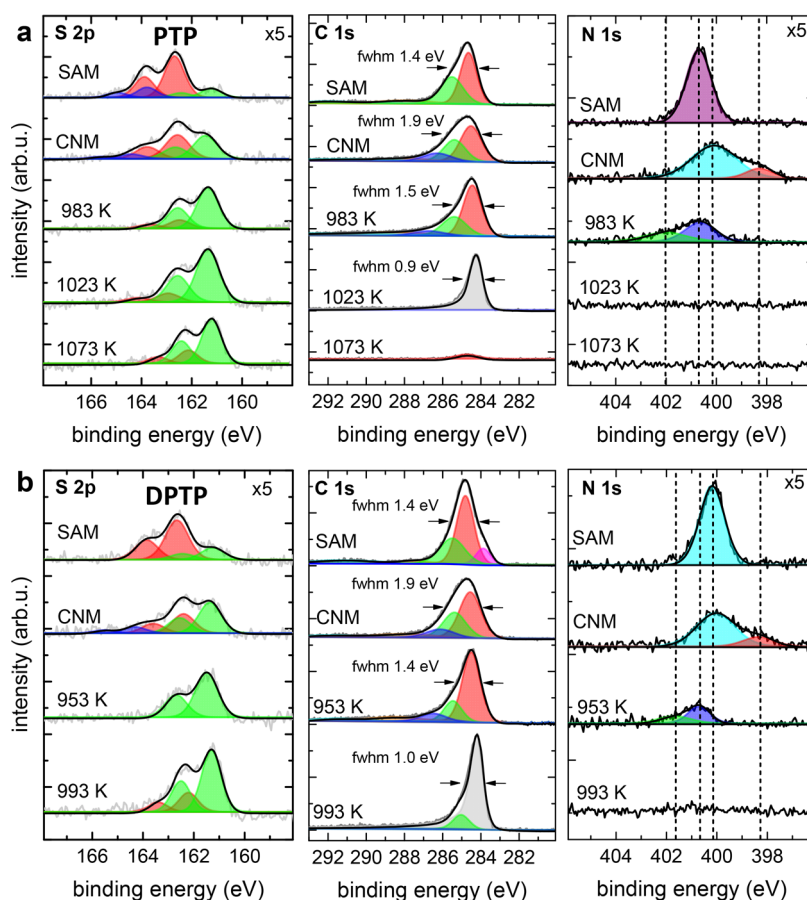


**Figure 3.** XPS characterization of the samples prepared from PTP (a) and DPTP (b) molecules on polycrystalline copper foils. For better representation, intensities of the S 2p spectra and N 1s spectra are multiplied by a factor of 5. The spectral resolution is 0.9 eV.

the modified chemical environment due to the additional methyl groups attached to the pyrrole ring of DPTP. The C/N ratios show the expected values of  $(10 \pm 2)/1$  (PTP) and  $(12 \pm 2)/1$  (DPTP). The estimated effective thickness of the SAMs is  $\sim 9$  Å for PTP SAM and  $\sim 8$  Å for DPTP SAM, which is in agreement with the structure of the DPTP SAMs in comparison to the TPP and PTP SAMs, resulting in a lower packing density.

**Cross-Linking of N-Containing Aromatic SAMs into Carbon Nanomembranes.** After electron irradiation induced cross-linking of the SAMs into the respective CNMs (see Figure 1a the step (i)  $\rightarrow$  (ii)) the S 2p, C 1s, and N 1s spectra show new features. Due to decomposition of the C–S bonds in the TPP SAMs during the cross-linking, the I(S 2p) of thiolates and copper sulfides changes to  $\sim 60\%$  and  $28\%$ , respectively, whereas the I(S 2p) of disulfide remains nearly unchanged (Figure 2a). The fwhm of the C 1s peak increases to 1.6 eV due to the additional carbon–nitrogen bonds created by cross-linking. These new species are reflected in the N 1s spectrum, where a new signal at 400.2 eV arises and can be attributed to amine, pyrrole, or azo groups (turquoise).<sup>20,33,36,37</sup> The pyridine peak at 398.5 eV decreases to  $\sim 60\%$  of the total N 1s intensity, whereas the intensity of the modified pyridine groups (brown) remains almost unchanged. The intensity of both the C 1s and N 1s peak decreases by  $\sim 10$ – $15\%$ , indicating some material desorption, which leads to a reduced thickness of  $8 \pm 1$  Å, and the C/N ratio changes to  $(15 \pm 3)/1$ . A structural change is also observed by the

disappearance of the LEED pattern, showing that the long-range order is absent in the formed TPP CNM.

The changes in the XP S 2p, C 1s, and N 1s spectra upon the electron irradiation induced cross-linking of structurally similar PTP and DPTP SAMs are shown in Figure 3a,b. These data enable us to reveal more detailed information about the process in general. Upon the cross-linking (see Figure 3a), the N 1s peak of the PTP CNM shifts by 0.6 eV to a lower BE of 400.1 eV (turquoise), which corresponds exactly to the BE of the N 1s peak of the DPTP SAM, Figure 3b. As this lower BE is attributed to the presence of methyl groups attached to the pyrrole ring in DPTP SAMs (see Figure 1d), this change provides direct spectroscopic evidence of the cross-linking between the individual molecules *via* formation of new C–C bonds between pyrrole rings and adjacent molecules in the PTP SAM. Additionally, a shoulder at a BE of 398.3 eV (red) arises in the N 1s spectrum, showing the formation of pyridine-like nitrogen.<sup>33,38</sup> This transformation indicates a conversion of some pyrrole groups into more stable pyridine groups comprising the conjugated system of three double bonds as in TPP (see Figure 1b–d). The total I(N 1s) constitutes  $\sim 80\%$  and  $\sim 20\%$  of the pyrrolic and pyridinic species, respectively. Most likely even more pyrrole groups are converted into other nitrogen species upon the cross-linking, as also modified pyridine groups<sup>34,35</sup> and tertiary nitrogen N–C<sub>3</sub><sup>39</sup> have similar BEs to the main peak found at 400.1 eV. Interestingly, the N 1s spectrum of the DPTP CNM shows the same features as the PTP CNM. As methyl groups are already bonded to the pyrrole group of the DPTP SAM, the cross-linking between the

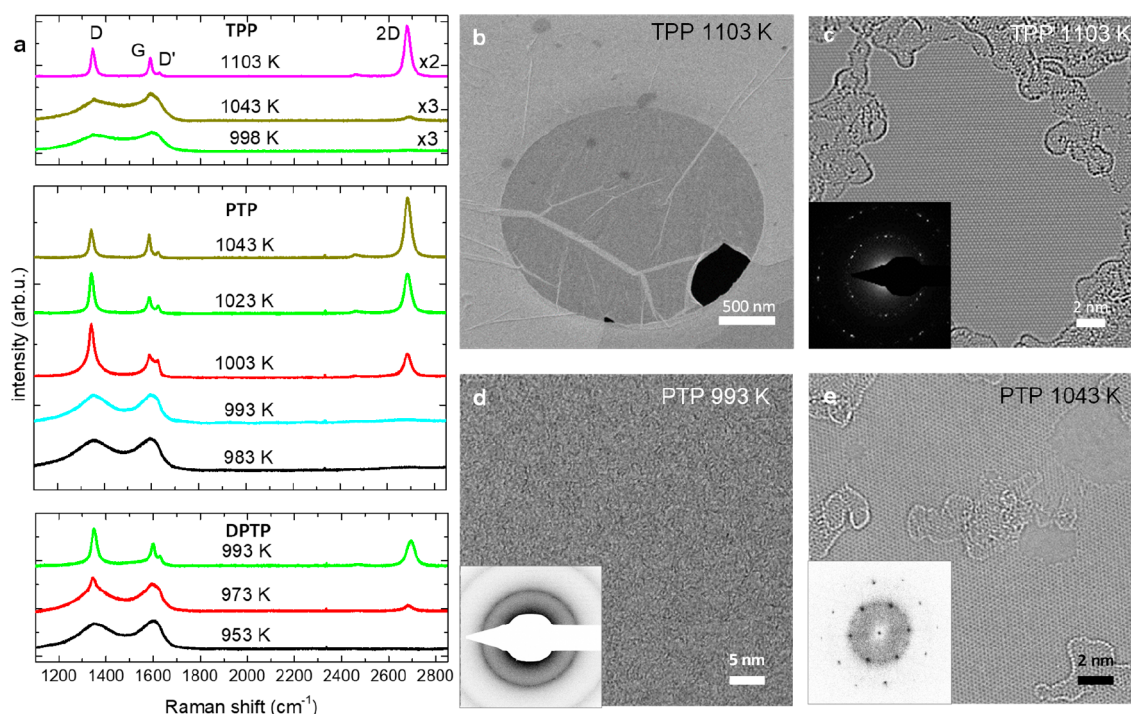


**Figure 4.** Structural characterization of the TPP, PTP, and DPTP CNMs pyrolyzed at different temperatures. (a) Raman spectra of the samples transferred onto SiO<sub>2</sub>/Si substrates after pyrolysis,  $\lambda = 532$  nm. (b) HIM image of a TPP sample transferred on a Quantifoil TEM grid after pyrolysis at 1103 K; no nanopores are detected. (c) HRTEM image of the sample in (b) demonstrating the formation of an almost single-layer graphene. The inset is a SAED pattern of the sample acquired over an area of  $\sim 1 \mu\text{m}^2$ . (d) HRTEM image of a PTP CNM pyrolyzed at 993 K. The inset shows the corresponding SAED pattern. (e) HRTEM image of a PTP CNM pyrolyzed at 1043 K; the inset shows the FFT of the image.

molecules does not affect the BE of the main peak in the N 1s spectrum. A shoulder at 398.3 eV indicates the formation of the pyridinic species with a comparable intensity ratio to the PTP CNM, Figure 3a,b.

The fwhm of the C 1s spectra for both PTP and DPTP samples increases to 1.9 eV upon the cross-linking, indicating the formation of new carbon species in the CNMs at a BE of 286.2 eV (blue). In comparison to the cross-linking of the TPP SAMs, this fwhm is noticeably broader, indicating a greater variety of the formed carbon species (see Figure 2 and Figure 3). As the sample preparation was performed in ultrahigh vacuum (UHV), the presence of C–O species having a similar BE can be excluded and, therefore, the peak at 286.2 eV can be assigned to the formation of new C–N bonds during the cross-linking.<sup>40,41</sup> The intensity of the main peak at 284.5 eV decreases by  $\sim 20\%$ , indicating a conversion of  $\text{sp}^2$ -carbon into the new C–N and  $\text{sp}^3$ -carbon species. The highlighted shoulder of the DPTP SAM (magenta) disappears after the cross-linking, and the PTP and DPTP CNMs qualitatively show the same C 1s spectrum. We observe some carbon and nitrogen desorption upon the cross-linking of the SAMs into CNMs. While the carbon signal is reduced by 5–10%, the reduction of nitrogen signal by 15–20% is more pronounced and leads to an increase of the carbon to nitrogen ratios in the PTP and DPTP CNMs to  $(12 \pm 3)/1$  and  $(16 \pm 3)/1$ , respectively. The effective thickness of the CNMs became reduced by  $\sim 1$  Å to 8 Å for PTP CNMs and to 7 Å for DPTP CNMs. The changes in the respective S 2p signals are similar to those described before for the TPP system (see Figure 2 and Figure 3).

### Conversion of N-Containing CNMs into Graphene.

#### TPP CNMs: Formation of Continuous Graphene Sheets.

Next, the N-containing CNMs were converted into graphene by vacuum pyrolysis. To induce this reaction, the samples were rapidly heated (within  $\sim 20$  min) to the target temperatures and then annealed for  $\sim 1$  h (see SI for details). We have found out that no significant conversion into graphene was observed for annealing temperatures below 900 K as well as that longer annealing times did not induce any further noticeable changes in the samples at all studied temperatures. First, we consider the evolution of the XP N 1s signal in the TPP CNM for different pyrolysis temperatures,  $T_p$ . After annealing at 713 K, a new nitrogen species at a BE of 401.6–402.0 eV (green), characteristic for the formation of graphitic nitrogen,<sup>42</sup> arises in the spectrum, Figure 2a, indicating first changes in the local chemical environment, which remain undetectable for Raman spectroscopy (see below). The pyridinic species (red) is still present in the spectrum, whereas the signal at 399.8 eV disappears. By increasing  $T_p$  to 1088 K, the amount of pyridine species continuously decreases and finally vanishes. For samples pyrolyzed at temperatures above 700 K, we attribute the nitrogen species at a BE of 400.5 eV to pyrrolic type of nitrogen.<sup>33,43</sup> Therefore, this species is marked in blue in comparison to the CNM data (turquoise), in which also other different nitrogen species might contribute to the N 1s signal. The ratio of the pyrrolic and graphitic types of nitrogen almost remains the same for all studied pyrolysis temperatures, whereas the total amount of nitrogen decreases significantly. In comparison to the SAM, only 20% of the nitrogen remains in the samples after pyrolysis at 1088 K. At this temperature the fwhm of the C 1s peak decreases from 1.6 eV to 1.1 eV, which

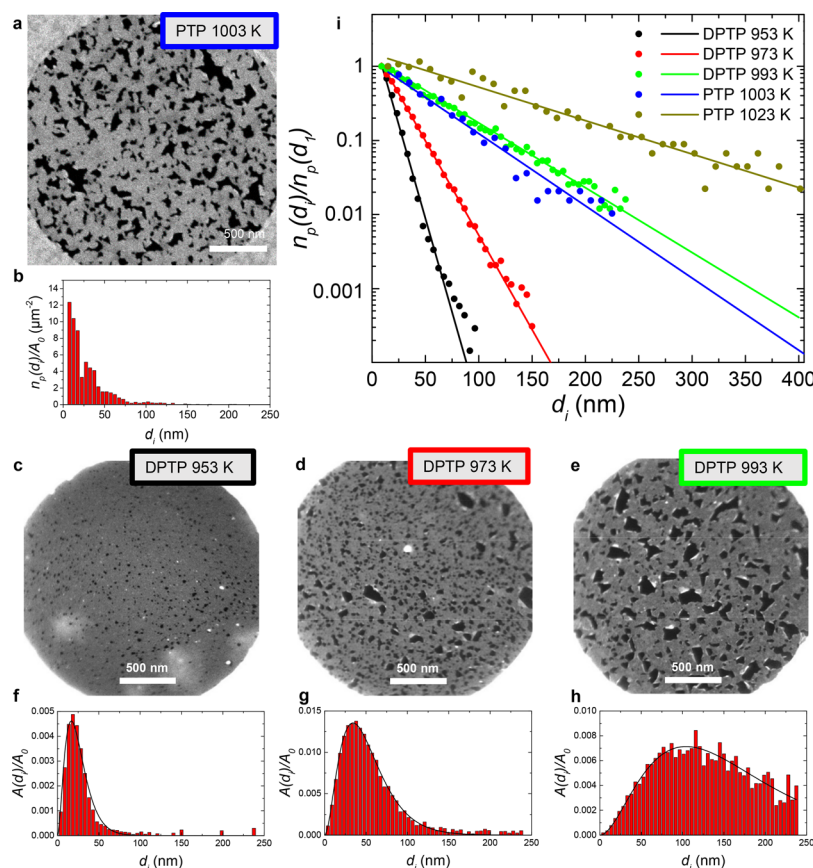


**Figure 5.** Quantitative analysis of the nanopores in PTP and DPTP samples pyrolyzed at different temperatures. (a) HIM micrograph of a PTP sample pyrolyzed at 1003 K showing the formation of nanopores. (b) Histogram representing the surface density of nanopores,  $n_p(d_i)$ , with a certain size  $d_i$  in the sample shown in (a). (c–e) DF-TEM images of DPTP samples pyrolyzed at 953, 973, and 993 K. (f–h) Histograms representing the contribution of the nanopore area of a certain size,  $A(d_i)$ , in (c)–(e) to the total sample area,  $A_0$ . (i) Summary of the nanopore density distribution,  $n_p(d_i)$ , in the PTP and DPTP samples as a function of the nanopore size. Here, the  $n_p(d_i)$  is normalized to the surface density of the first bin,  $n_p(d_1)$ , for respective samples. In (b) and (f)–(i) the bin width is 5 nm.

is typical for the conversion of CNMs into graphene.<sup>29</sup> The formation of graphene is further indicated by a direct structural observation presented in Figure 2b (iv). The corresponding LEED pattern represents a graphene superlattice formed on Cu(111) with a length of the unit cell of 6.75 Å and a rotational angle of 19.1°;<sup>29</sup> see Figure 2b (v,vi). The conversion of TPP CNMs into graphene at higher temperatures was also studied on polycrystalline copper foils. Figure S1 shows the C 1s, N 1s, S 2p, and O 1s spectra after the self-assembly, cross-linking, and pyrolysis at 1103 K. At higher pyrolysis temperatures, the fwhm of the C 1s peak decreases further to 0.9 eV, and its shape can be well described by a Doniach–Sunjic line shape with an asymmetry factor  $\alpha = 0.12$ , as typical for graphene.<sup>44</sup> Simultaneously, the N 1s signal vanishes completely from the spectrum and the S 2p signal only consists of copper sulfide species; no oxygen was observed in these spectra for all conversion steps.

To further characterize the conversion of TPP CNMs into graphene, we employed Raman spectroscopy, scanning electron microscopy (SEM), HIM, and HRTEM. The Raman spectroscopy data presented in Figure 4a demonstrate that at a low  $T_p$  of 998 and 1043 K nanocrystalline graphene forms. The characteristic spectroscopic features show a low-intensity 2D-band as well as a broad D-band and G-band at  $1372 \pm 1$  and at  $1591 \pm 1$   $\text{cm}^{-1}$ ,<sup>23,28,29</sup> respectively. The pyrolysis at a higher temperature of 1103 K results in the

formation of single-layer graphene with a significantly higher crystallinity, which is reflected in a symmetric 2D peak at  $2680 \pm 1$   $\text{cm}^{-1}$  and an  $I(2D)/I(G)$  ratio of  $\sim 3:1$ .<sup>45</sup> To study this structural transformation, the pyrolyzed samples were transferred onto TEM grids. SEM images for the samples pyrolyzed at 998 and 1043 K enable visualizing directly the conversion into graphene. The formation of graphene is observed as the appearance of bright areas within the darker CNM background (see Figure S3), which is due to a higher secondary electron yield from the conductive graphene areas in comparison to the insulating TPP CNM. Figure 4b presents a HIM image of the sample annealed at 1103 K, showing the formation a continuous film, which is identified unambiguously by HRTEM and selected area electron diffraction (SAED) as a polycrystalline single-layer graphene, Figure 4c. For all samples prepared by pyrolysis of TPP CNMs the formation of continuous graphene sheets was observed, as shown in Figure 4b and Figure S3.

**PTP and DPTP CNMs: Formation of Nanoporous Graphene Sheets.** Similar to TPP CNMs, PTP and DPTP CNMs were also converted into graphene *via* pyrolysis. Figure 3 shows the respective XPS data after the conversion at different temperatures. For temperatures of  $\sim 950$ – $980$  K, the respective N 1s signals for both types of CNMs reveal the presence of two nitrogen species: one at a BE of 400.7 eV (blue), which can be attributed to pyrrole or tertiary



nitrogen,<sup>36,39,40,43</sup> and another one at a BE of 401.6–402 eV (green), due to the formation of graphitic nitrogen.<sup>42</sup> The graphitic nitrogen constitutes ~40% of the total N 1s intensity. Note that pyridinic nitrogen, which is present in the nonannealed CNMs (turquoise), vanishes after annealing at these temperatures. The fwhm of the C 1s signal decreases to ~1.4–1.5 eV, whereas the relative intensity of the sp<sup>2</sup>-carbon component (284.4 eV, red) increases to 60–70% of the total intensity. Simultaneously, the intensity of the other components due to C–S bonds (285.4 eV, green) and C–N bonds (286.5 eV, blue) decreases to 20–30% and to 10%, respectively. This behavior is very similar to the results discussed above for the TPP CNMs (see Figure 2a) and shows the formation of nanocrystalline graphene, which is further confirmed by the respective Raman spectra and TEM data presented in Figure 4a and d, respectively.

As can be seen from the complementary XPS, Raman spectroscopy, and TEM data (see Figures 3 and 4), and as observed for the TPP samples on copper foils, annealing of the PTP and DPTP samples at higher temperatures results in their transformation into single-layer graphene with a higher crystallinity and in simultaneous desorption of nitrogen. However, in comparison to TPP this transformation occurs at about 50–100 K lower temperatures. We attribute this behavior to a lower thermal stability of the pyrrole groups in comparison to the pyridine groups as well as to a lower surface density of carbon in the structurally similar PTP and DPTP CNMs in comparison to the TPP CNMs. In the DPTP CNMs, having a lower surface density in comparison to the PTP CNMs, the conversion into graphene is shifted by about 10 K toward lower temperatures. Interestingly, at the highest  $T_p$  = 1073 K applied to PTP samples the intensity of the XP C 1s signal disappears nearly completely (see Figure 3a), indicating either desorption of the formed graphene layer or its dissolution in the copper substrate. A detailed analysis of the respective XPS and Raman spectroscopy data (Figures 3 and 4) is presented in the SI (pp 8, 9 and Tables S1–S5).

Next, we concentrate on the HRTEM data of the PTP sample annealed at 1043 K, Figure 4e. In contrast to the data for a TPP sample (Figure 4c), where the formation of continuous graphene sheets was observed, several pores with nanometer dimensions can be recognized in the formed single-crystalline graphene area. The presence of nanopores in the graphene formed by pyrolysis of the PTP and DPTP CNMs is also clearly detected by HIM and dark field TEM (DF-TEM) (see Figure 5). In the following section, we provide a detailed analysis of the nanopores' size and distribution depending on the pyrolysis temperature of PTP and DPTP CNMs employing complementary TEM, HIM, SEM, and AFM measurements.

**Quantitative Characterization of the Formed Nanopores.** First, we investigate the formation of nanoporous graphene by pyrolysis of PTP CNMs. Initially, for a low pyrolysis temperature of 993 K, a continuous film of nanocrystalline graphene is formed (see HRTEM and HIM images in Figure 4d and Figure S4a, respectively). However, an increase of  $T_p$  to 1003 K, at which graphene with higher crystallinity is formed (see Raman spectroscopy data in Figure 4a), leads to the formation of nanopores as shown in Figure 5a, presenting a HIM image of the respective freestanding sheet. The formation of the nanopores after pyrolysis can also be detected directly on the polycrystalline copper foils (Figure S4b). Comparing these data with the same PTP sample after its transfer onto a TEM grid, the size and shape of the formed

graphene pores are found to be the same, Figure S4c. These results demonstrate that the pore formation is an intrinsic property of the pyrolytic conversion of PTP CNM into graphene. We attribute the formation of nanopores here, in comparison to the formation of continuous graphene sheets by pyrolysis of the TPP CNMs, to both a lower amount of carbon in PTP in comparison to TPP (see Figure 1b) and a higher thermal stability of the pyridine group in TPP in comparison to the pyrrole group in PTP. Thus, during the pyrolysis of PTP CNMs, desorption of nitrogen atoms in combination with a lower amount of carbon atoms hinders the growth of a continuous graphene sheet and favors the nanopore formation.

Similar to PTP, DPTP samples also show the formation of nanopores upon pyrolysis, Figure 5c–e. However, due to a lower packing density of the DPTP SAM in comparison to the PTP SAM and due to the desorption of the methyl groups upon the formation of the DPTP CNMs (see previous XPS analysis), the carbon density in this system is lower, which favors the formation of nanopores also at a lower  $T_p$  = 953 K. As can be seen from the DF-TEM data, Figure 5c–e, by increasing  $T_p$  to 993 K, the nanopore sizes and density evolve toward higher values.

To quantitatively evaluate the size and the surface density of the nanopores in the formed graphene sheets, HIM and DF-TEM images were processed employing image analysis software<sup>46</sup> (see also Figure S5a and SI p 9). In this procedure, we approximated nanopores with circular shapes, which enabled us to obtain the nanopore surface density,  $n_p$ , as a function of their diameter,  $d$ . The result of this assessment for a PTP sample in Figure 5a is presented in Figure 5b as a histogram with a bin width of 5 nm. The numerical analysis shows that  $n_p(d)$  decreases exponentially with increasing nanopore diameter (see SI pp 9–11 for details). Similar exponential dependencies were found for all nanoporous graphene sheets obtained by pyrolysis of the PTP and DPTP CNMs (see SI Figure S6). These data are summarized in Figure 5i. To enable a comparison of different samples, the surface density,  $n_p(d_i)$ , was normalized by the surface density of the first bin,  $n_p(d_1)$ , and plotted on a logarithmic scale. It can be seen that the nanopore size and surface density depend strongly on the pyrolysis temperature: with increasing temperature larger pores are formed and the distribution becomes broader. In order to represent the contribution of nanopores with a certain size  $d_i$  to the porosity of the graphene samples, their total surface area,  $A(d_i)$ , was normalized by the sample area,  $A_0$  (see SI pp 9, 10) and plotted as histograms in Figure 5f–h. These histograms are placed below the respective microscopy images. From the distribution functions of the nanopore surface density, plotted in Figure 5f–h with blue curves, the mean values for the nanopore diameter, their standard deviation, and the porosity ( $\eta = \frac{\sum A(d_i)}{A_0}$ ) of the formed graphene sheets can be obtained. Thus, for graphene sheets formed from DPTP CNMs by pyrolysis at 953, 973, and 993 K (Figure 5c–e) the mean nanopore diameter,  $d_{\text{mean}}$ , is  $25 \pm 15$ ,  $51 \pm 30$ , and  $156 \pm 91$  nm, and the porosity is  $0.03 \pm 0.01$ ,  $0.19 \pm 0.02$ , and  $0.31 \pm 0.03$ , respectively. For the latter sample the formation of a few large pores with diameters > 200 nm leads to a significant increase of both values. The respective data on the mean nanopore diameter and the porosity PTP CNMs pyrolyzed at 1003 and 1023 K are  $120 \pm 40$  nm ( $\eta = 0.26 \pm 0.03$ ) and  $285 \pm 152$  nm ( $\eta = 0.41 \pm 0.05$ ), respectively. An increase of the porosity for the PTP CNMs

pyrolyzed at 1023 K results in the formation of graphene sheets resembling a network of interconnected graphene nanoribbons (see Figure S4b–d). It is striking that these graphene samples are mechanically stable as freestanding sheets, although the narrowest interconnects have a width below 20 nm.

Complementary to the evaluation of nanopores in suspended graphene sheets, we also analyzed supported graphene sheets on solid substrates using AFM and HIM. By employing the same statistical analysis, the pore distribution was studied (Figure S7). In comparison to the suspended graphene sheets, we detected a smaller amount of large nanopores. We attribute this difference to ruptures of the freestanding graphene sheets due to the residual strain and microfabrication.<sup>47</sup> Thus, the obtained mean diameter of the nanopores in the supported graphene sheets prepared by pyrolysis of the DPTP CNM at 993 K is  $79 \pm 46$  nm, which is significantly smaller in comparison to the suspended membrane ( $d_{\text{mean}} = 156 \pm 91$  nm).

**Charge Carrier Transport in the Formed Graphene Sheets.** Next, we analyzed electronic properties of the pyrolyzed CNMs by studying under vacuum their room temperature (RT) sheet resistivity,  $\rho$ , and electric field-effect mobility,  $\mu_{\text{FE}}$ , Figure 6. To this end, four-point measurements of the continuous sheets, transferred onto SiO<sub>2</sub>/Si wafers, as well as two-point measurements of microfabricated FET devices were conducted employing a probe station (see SI pp 8, 9). By conversion of the insulating PTP and DPTP CNMs into graphene,  $\rho$  decreases from  $>10^8$  k $\Omega$ /sq to about  $\sim 100$  k $\Omega$ /sq and  $\mu_{\text{FE}}$  increases from  $10^{-3}$  cm<sup>2</sup>/(V s) to  $\sim 200$  cm<sup>2</sup>/(V s) for samples with low and high pyrolysis temperatures ( $T_p \approx 950$ – $1050$  K), respectively (see Figure 6a and SI pp 13, 14). The  $\rho(T_p)$  and  $\mu_{\text{FE}}(T_p)$  dependencies correlate well with the structural and chemical changes observed upon pyrolysis by Raman spectroscopy, LEED, HRTEM, and XPS (Figures 2–4). These spectroscopy and microscopy data show a gradual conversion of molecular short-range ordered CNMs into graphene with increasing crystallinity with higher  $T_p$ . A detailed analysis of the field-effect data has revealed two different electric carrier transport mechanisms in the samples with low and high  $T_p$ , Figure 6b,c and Figure S8. As shown in Figure 6b, for a sample with a low degree of conversion into graphene, the electric field effect is well described by the variable range hopping (VRH) model, which was earlier developed for studying the charge carrier transport in nanocrystalline single-layer graphene sheets.<sup>28</sup> Here, the respective dependence of the conductivity on gate voltage,  $V_G$ , is given by  $\ln \frac{\sigma(V_G - V_G^*)}{\sigma(0)} \propto (V_G - V_G^*)$ , where  $\sigma$  is the electrical conductivity and  $V_G^*$  is the gate voltage at minimum conductivity of the sample. The transport in samples with a higher degree of the conversion into graphene follows a typical relationship for single-layer graphene sheets,<sup>48</sup> Figure 6c. Here, the conductivity as a function of the applied gate voltage, *i.e.*, the charge carrier concentration,  $n$ , is well described by<sup>49</sup>

$$\sigma(n)^{-1} = (ne\mu_l)^{-1} + \sigma_s^{-1} \quad (1)$$

with  $n = \sqrt{(V_G - V_D)^2 C_G^2 / e^2 + n^{*2}}$ , where  $e$  is the electron charge,  $\mu_l$  is the long-range scattering mobility,  $\sigma_s$  is the carrier-density-independent conductivity due to short-range scattering,  $V_D$  is the gate voltage at the Dirac point,  $C_G$  is the gate capacitance, and  $n^*$  is the effective residual charge carrier

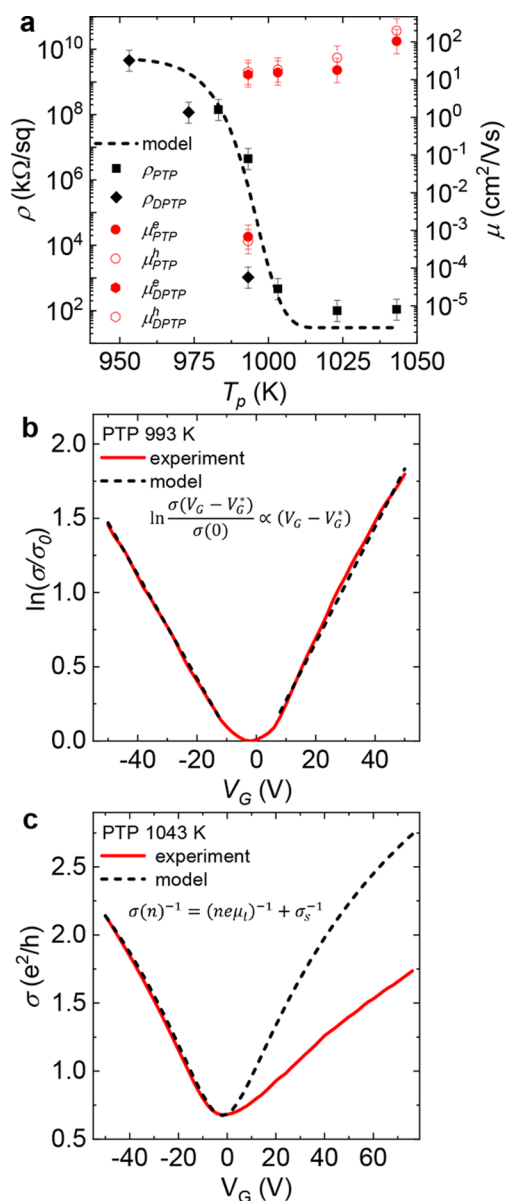


**Figure 6.** Charge carrier transport in graphene samples synthesized by pyrolysis of PTP and DPTP CNMs. (a) Room-temperature sheet resistivity,  $\rho$ , and electric field-effect mobility,  $\mu_{\text{FE}}$ , of the samples measured in a vacuum as a function of the pyrolysis temperature,  $T_p$ . The mobility values for electrons and holes are shown with the solid and open signs, respectively. Ambipolar transport characteristics of graphene samples formed by the pyrolysis of PTP CNMs at 993 K (b) and 1043 K (c). For more details, see the text.

concentration at the Dirac point.<sup>50</sup> An asymmetry in the electric field effect for holes and electrons observed in Figure 6c is attributed to the interaction of graphene with metal contacts in the studied FET devices.<sup>51</sup> By applying eq 1 to the hole transport characteristic in Figure 6c, we obtain a value of 500 cm<sup>2</sup>/(V s) for  $\mu_l$ , with the respective parameters of  $\sigma_s = 5.2$  e<sup>2</sup>/h and  $n^* = 37.5 \times 10^{10}$  cm<sup>-2</sup>. A summary of the  $\mu_l$ ,  $\sigma_s$ , and  $n^*$  data for other studied samples is shown in SI Table S6. For all samples, the obtained  $\mu_l$  values are significantly higher than the respective  $\mu_{\text{FE}}$  values. Such a difference indicates that the charge carrier mobility in the formed graphene sheets is strongly influenced by residual charges and short-range



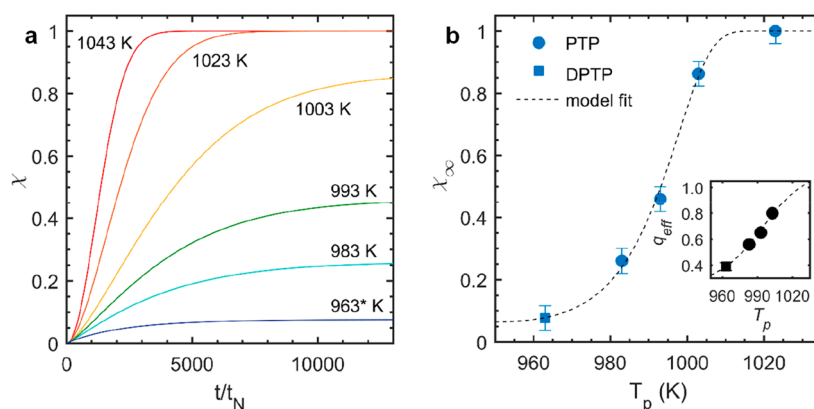


**Figure 7.** Kinetics of the conversion of CNMs into graphene calculated by the modified KJMA model. (a) Calculated crystallinity as a function of time and pyrolysis temperatures,  $\chi(t, T_p)$ . (b) Dashed line: Calculated asymptotic crystallinity as a function of pyrolysis temperature,  $\chi_\infty(T_p)$ . Blue symbols: Experimental  $\chi_\infty(T_p)$  data obtained from XPS. The inset shows the effective growth exponent,  $q_{\text{eff}}(T_p)$ , (dashed line) calculated from the experimental crystallinity data and the kinetic growth model (black symbols).

scattering processes. We attribute the latter predominantly to the presence of nanopores. Moreover, the presence of nanopores results also in the underestimation of the intrinsic  $\mu_1$  values by eq 1. Taking the experimentally determined porosity values into account, a  $\mu_1$  higher than 600 cm<sup>2</sup>/(V s) can be expected in the nanoporous graphene networks formed by the highest  $T_p$  (see Table S6).

To analyze the experimental  $\rho(T_p)$  data upon conversion of insulating CNMs into conducting graphene (Figure 6a) quantitatively, we apply an electrical percolation model, as introduced for the description of systems with an insulator to metal transition.<sup>52–55</sup> In this model, conductivity,  $\sigma$ , is given for a percolating electrical network as a function of crystallinity,  $\chi$ . The formation of graphene areas embedded into a CNM matrix upon pyrolysis is observed in our study by both SEM and HRTEM (see Figure S3c and Figure S9). It was reported also earlier for the pyrolysis of 1,1'-biphenyl-4-thiol-based CNMs on Cu(111) by atomically resolved scanning tunneling microscopy (STM).<sup>29</sup> We define the sample crystallinity for a certain  $T_p$  as  $\chi(T_p) = A_{\text{Gr}}(T_p)/(A_{\text{CNM}}(T_p) + A_{\text{Gr}}(T_p))$ , where  $A_{\text{CNM}}(T_p)$  and  $A_{\text{Gr}}(T_p)$  are the CNM and graphene areas after pyrolysis of a sample, respectively. While  $\chi(T_p)$  is independent of porosity, the presence of nanopores reduces the  $\sigma(T_p)$  values by a factor of  $(1 - \eta(T_p))$  (see SI pp 14). Taking the  $\eta(T_p)$  values into account, we obtain for  $\sigma(T_p)$

$$\log \frac{\sigma(T_p)}{1 - \eta(T_p)} = \log \frac{\sigma_l}{1 - \eta_l} + \left( \log \frac{\sigma_h}{1 - \eta_h} - \log \frac{\sigma_l}{1 - \eta_l} \right) \times \frac{f(\chi(T_p)) - f(\chi_l)}{f(\chi_h) - f(\chi_l)} \quad (2)$$

where  $f(\chi) = \frac{1}{1 + e^{b(\chi(T_p) - \chi_c)}}$ ,  $l$  and  $h$  are the indices for the respective values of the samples with the lowest or highest crystallinity,  $\chi_c$  is the percolation threshold, and  $b$  is an empirical model parameter. In order to employ eq 2 for description of the experimental  $\sigma(T_p)$  data, we use the  $\chi(T_p)$  values obtained from analysis of the respective sp<sup>2</sup>/sp<sup>3</sup> ratios in the photoelectron C 1s peaks (see SI Section 6, Table S7). We assign the lowest and the highest crystallinity to the pyrolyzed DPTP and PTP CNMs at a  $T_p$  of 953 and 1043 K, respectively. For the percolation threshold value we use  $\chi_c = 0.5$ , as obtained from the  $\sigma(T_p)$  data for samples with the highest and lowest conductivity (see SI Section 7 for details).

Employing these parameters and  $b = 3$ , the experimental  $\sigma(T_p)$  data can be described very well by eq 2 (see SI Figure S10 and SI Table S8). Based on these results, the dashed line in Figure 6a represents the calculated  $\rho(T_p)$  values. The model describes very well the experimental data in a broad range, within 8 orders of magnitude, for all pyrolysis temperatures. It corresponds also very well to the experimentally observed electrical field-effect data, which reveal VRH transport in samples with crystallinity below  $\chi_c$  (see Figure 6b) and the characteristic graphene transport in samples with crystallinity above  $\chi_c$  (see Figure 6c and SI Tables S6, S7).

**Kinetic Model Description of the Conversion of CNMs into Graphene via Pyrolysis.** Our complementary XPS, Raman spectroscopy, HRTEM, and electric transport data (Figures 2–4, 6) show that (i) CNMs are converted into graphene at temperatures above 950 K, (ii) for a respective pyrolysis temperature only a certain degree of the conversion is achieved, independent of the pyrolysis time (even after >1 h no further changes could be observed), and (iii) graphene nuclei grow within the CNM matrix. A similar crystallization behavior was reported previously by Mattoni and Colombo for the conversion of an amorphous covalently bound silicon film into its crystalline phase.<sup>31,56</sup> Their molecular dynamics (MD) simulations have shown that the formation of defects at the solid/solid crystallization front hinders the growth of the crystalline phase, which results in a certain asymptotic crystallinity  $\chi < 1$  for a given transformation temperature below a material-specific threshold temperature. Based on these results a modified KJMA model for the growth of the crystalline phase was developed.<sup>31</sup> We adopt this model to describe the conversion of molecular, covalently bonded CNMs into graphene (see SI Section 8). Within this model, the crystallinity of the system as a function of time,  $t$ , and  $T_p$  is presented by

$$\chi(t, T_p) = \chi_\infty(T_p) \left[ 1 - \exp \left( - \frac{1}{\chi_\infty(T_p)} \int_0^t \pi \Gamma^{2q(T_p)} \chi^2 t^{2q(T_p)} J(t - \tau) d\tau \right) \right] \quad (3)$$

where  $\chi_\infty(T_p)$  is the asymptotic crystallinity,  $\Gamma$  is the characteristic frequency,  $\lambda$  is the characteristic length for the exchange at the interface between the disordered and the crystalline phase,  $J(t) = J_0(h(t) - h(t - t_N))$  is the nucleation

rate per area,  $h(t)$  is the Heaviside step function,  $t_N$  is the nucleation time, and  $q(T_p)$  is the growth exponent.

To calculate the crystallinity with eq 3, we employed both the experimental data of this study and some model parameters from ref 31. We obtained the nucleation rate  $J_0 = 10^{12} \mu\text{m}^{-2} \text{s}^{-1}$  by analyzing the size of the crystallites in the HRTEM images (see SI Figure S9) and assuming a circular shape of the nuclei. Thus, for a PTP sample pyrolyzed at  $T_p = 993 \text{ K}$  the asymptotic crystallite radius of  $R_\infty \approx 10 \text{ nm}$  was extracted, giving a concentration of nuclei of  $n_{\text{cr}} = \frac{\chi_\infty}{\pi R_\infty^2} \approx 1000 \mu\text{m}^{-2}$ , where  $\chi_\infty = 0.46$  (see SI Table S7). In this way the nucleation rate can be estimated as  $J_0 = \frac{n_{\text{cr}}}{t_N}$ . Based on previous values determined for silicon, we use the values of  $\Gamma$ ,  $\lambda$ , and  $t_N$  of  $0.01 \text{ ns}^{-1}$ ,  $8 \text{ nm}$ , and  $1 \text{ ns}$  as obtained by MD simulations in ref 31. According to the same study, the growth exponent  $q(T_p)$  in eq 3 is presented by

$$q(T_p) = c_1 + c_2 \left\{ \frac{1}{2} + \frac{1}{\pi} \tan^{-1} \left[ c_3 \left( \frac{T_p}{T^*} - 1 \right) \right] \right\} \quad (4)$$

where  $c_1$ ,  $c_2$ , and  $c_3$  are the model parameters and  $T^*$  is the characteristic threshold temperature above which complete conversion is observed. For modeling the conversion kinetics of CNMs into graphene upon pyrolysis, we have considered  $c_1$ ,  $c_2$ , and  $c_3$  values of 0.0841, 1.49, and 16.34, as obtained by MD simulations for silicon.<sup>31</sup> Based on the XPS measurements,  $T^*$  was fixed at 1020 K. With this data set, the calculated crystallinity upon conversion of CNMs into graphene at different  $T_p$  is shown in Figure 7a. For this representation, mainly the data for PTP samples were used with the exception of one data point for DPTP at 953 K. In this system the conversion sets in at  $\sim 10 \text{ K}$  lower temperature in comparison to PTP CNMs; therefore this data point was corrected to 963 K for consistency. As can be seen from Figure 7a, the kinetics of conversion increases with increasing  $T_p$ ; for  $T_p \leq 1003 \text{ K}$  a complete conversion into graphene is not achieved.

In order to obtain the asymptotic crystallinity for any  $T_p$ , we set  $\chi_\infty(T_p) = 1$  in eq 3, and by fitting the  $\chi(t_\infty, T_p)$  values to the  $\chi_\infty(T_p)$  data extracted from XPS we obtain the function  $q_{\text{eff}}(T_p)$  (see SI pp 18). These data are presented in Figure 7b as an inset. Using eq 3 it is now possible to predict the asymptotic crystallinity of the samples at any  $T_p$ , Figure 7b. Note that according to the model calculation in Figure 7a, a difference in the crystallinity of the samples pyrolyzed at 1023 and 1043 K can be expected (see also SI Table S9). This difference can be indeed observed in the Raman spectra of the formed graphene sheets, showing a higher ratio of  $I(2D)/I(G)$  and a lower ratio of  $I(D)/I(G)$  for the PTP samples pyrolyzed at 1043 K in comparison to 1023 K, Figure 4a. According to Figure 7a, another interesting consequence is a possibility to tune the crystallinity and therewith the size of the formed graphene islands in the insulating CNM matrix either by pyrolysis temperature or by pyrolysis time. In this way it should be feasible to employ both these parameters to form graphene quantum dots embedded into CNMs. Such composite materials can possess a variety of useful functional properties for catalytic and photonic applications.

## CONCLUSIONS

We have presented a method to synthesize nanoporous single-layer graphene sheets with tunable crystallinity and porosity.

To this end, nitrogen-containing aromatic compounds were self-assembled into monolayers on copper substrates, cross-linked *via* low-energy electron irradiation into covalently bound molecular nanosheets, and pyrolyzed under vacuum. We have analyzed all steps of this synthetic method by complementary spectroscopy, microscopy, and diffraction methods as well as by electric transport measurements. The presence of nitrogen in the molecular precursors (pyridine and pyrrole groups) has allowed us to follow the atomistic details of the cross-linking by photoelectron spectroscopy. Due to dissociation of the carbon–nitrogen bond and desorption of nitrogen at pyrolysis temperatures, the choice of precursor compounds with a specific molecular structure enables us to produce either highly crystalline continuous sheets or nanoporous sheets of single-layer graphene. The porosity and the crystallinity of the formed graphene can be adjusted *via* pyrolysis temperature. The formed nanoporous graphene sheets resemble a percolated network of mechanically stable graphene nanoribbons and demonstrate attractive electronic properties. They show a strong electric field effect with a mobility of the charge carriers estimated as  $\sim 600 \text{ cm}^2/(\text{V s})$ . Such electronic characteristics make the synthesized nanoporous single-layer graphene sheets an attractive material for sensor applications in graphene-based field-effect devices. We expect that the edges in the nanoporous graphene sheets can be functionalized with specific chemical or biochemical probe molecules without degrading the overall electronic properties. Moreover, the applied model description of the electric charge transport and the growth kinetics suggests that the developed synthesis method may enable the generation of graphene quantum dots in an insulating 2D molecular matrix by tuning the pyrolysis conditions. These materials can have a variety of applications in catalysis and nanophotonics.

## MATERIALS AND METHODS

**Sample Preparation.** The molecular TPP, PTP, and DPTP compounds were synthesized according to the procedures described in detail in the SI. Afterward SAMs were prepared on copper substrates by vapor deposition in a multichamber UHV system. Cross-linking into CNMs was achieved under UHV conditions ( $<10^{-9} \text{ mbar}$ ) using an electron energy of 50 eV and a dose of  $60 \text{ mC/cm}^2$ . Pyrolysis of the CNMs leading to the conversion into graphene was conducted in the same UHV system on a heatable/cooleable manipulator for  $\sim 1 \text{ h}$  using rapid heating and cooling (within 20 min). Transfer of the graphene monolayers was conducted using a poly(methyl methacrylate) (PMMA)-based transfer protocol onto  $\text{SiO}_2$  wafers and TEM grids (see, e.g., ref 57). See SI for details of the sample preparation.

**Characterization.** The as-grown SAMs, CNMs, and graphene monolayers were characterized by XPS and LEED *in situ* in a multichamber UHV system (Omicron Nanotechnology). XPS was performed using a monochromatic X-ray source (Al  $K\alpha$ ) and an electron analyzer (Sphera) with a resolution of 0.9 eV. LEED patterns were recorded with a BDL600IR-MCP instrument (OCI Vacuum Microengineering) using a multichannel plate (MCP) detector with electron beam currents below 1 nA. After sample transfer, Raman spectroscopic measurements were carried out using a commercial micro-Raman device (HR LabRam inverse system, JobinYvon Horiba) with a frequency-doubled Nd:YAG laser ( $\lambda = 532 \text{ nm}$ ) employing a 100 $\times$  objective and a Peltier-cooled back-illuminated CCD camera with a resolution of  $1.3 \text{ cm}^{-1}$ . HIM measurements were carried out with a Carl Zeiss Orion Plus microscope operated at  $\sim 35 \text{ kV}$  acceleration voltage at currents of 0.2–0.5 pA. Secondary electrons were collected by an Everhart-Thornley detector. The SEM images were taken with a Zeiss Sigma VP at a beam energy of 10 kV and use of an in-lens detector. The AFM measurements were conducted using

an Ntegra (NT-MDT) in semicontact mode at ambient conditions. AC-HRTEM, dark-field TEM, and electron diffraction were performed in an FEI Titan 80-300 kV TEM with  $C_s$  correction, as well as in the  $C_s/C_c$ -corrected “SALVE” FEI Titan Themis cubed TEM. Both microscopes were operated at a low acceleration voltage of 80 kV to prevent knock-on damage in the graphene membranes. The electrical characterization was carried out after lithographical fabrication of FET devices on  $\text{SiO}_2/\text{Si}$  wafers inside a Lakeshore TTPX needle probe station under vacuum using Keithley 2634B source measure units. The full methods description is available in the SI.

## ASSOCIATED CONTENT

### Supporting Information

The Supporting Information is available free of charge on the ACS Publications website at DOI: 10.1021/acsnano.9b03475.

Full description of sample preparation and methods, interpretation of XPS spectra, data analysis of the nanopores and the modeling of the XPS, Raman and electrical conductivity data, kinetic model, and supporting references (PDF)

## AUTHOR INFORMATION

### Corresponding Authors

\*E-mail: [aterfort@chemie.uni-frankfurt.de](mailto:aterfort@chemie.uni-frankfurt.de).

\*E-mail: [andrey.turchanin@uni-jena.de](mailto:andrey.turchanin@uni-jena.de).

### ORCID

Armin Götzhäuser: 0000-0002-0838-9028

Andreas Terfort: 0000-0003-2369-5151

Andrey Turchanin: 0000-0003-2388-1042

### Author Contributions

A.Tu. designed and directed the research. A.Te. and M.F. designed and synthesized the precursor molecules for the growth of graphene sheets. C.N., N.-E.W., and O.R. conducted and analyzed XPS, Raman spectroscopy, and LEED measurements. M.J.M. performed and analyzed TEM measurements. U.K. supervised the TEM work. C.N. performed and analyzed HIM measurements. A.G. supervised the HIM study. T.W. fabricated field-effect devices. C.N. and D.K. performed electrical measurements and analyzed the data. C.N. and M.J.M. analyzed the sample porosity. D.K. and A.Tu. developed the electric transport and the kinetic model description. C.N., D.K., and A.Tu. wrote the manuscript. All authors contributed to the discussion of the results and the manuscript.

### Notes

The authors declare no competing financial interest.

## ACKNOWLEDGMENTS

We acknowledge financial support of the Deutsche Forschungsgemeinschaft (DFG) through SPP 1459 “Graphene” (TU149/2-2, KA1295/19-2), Heisenberg Programm (TU149/3-1), research grant TU149/5-1, research infrastructure grant INST 275/25 7-1 FUGG, and “ProExzellenz 2014-2019” grant of the Thüringer MWWG. This project has also received funding from the European Union’s Horizon 2020 research and innovation program under grant agreement Nos. 696656 and 785219. M.F. thanks the Fonds der Chemischen Industrie for a stipend. We thank Stephanie Höppener and Ulrich S. Schubert for enabling the SEM characterization, Jürgen Popp for the possibility of Raman spectroscopy measurements, and Zian Tang for technical support. The SEM facilities of the Jena

Center for Soft Matter (JCSM) were established with a grant from the German Research Council (DFG).

## REFERENCES

- (1) Novoselov, K. S.; Geim, A. K.; Morozov, S. V.; Jiang, D.; Zhang, Y.; Dubonos, S. V.; Grigorieva, I. V.; Firsov, A. A. Electric Field Effect in Atomically Thin Carbon Films. *Science* **2004**, *306*, 666–669.
- (2) Novoselov, K. S.; Mishchenko, A.; Carvalho, A.; Castro Neto, A. H. 2D Materials and van der Waals Heterostructures. *Science* **2016**, *353*, aac9439.
- (3) Ferrari, A. C.; Bonaccorso, F.; Fal’ko, V.; Novoselov, K. S.; Roche, S.; Boggild, P.; Borini, S.; Koppens, F. H. L.; Palermo, V.; Pugno, N.; Garrido, J. A.; Sordan, R.; Bianco, A.; Ballerini, L.; Prato, M.; Lidorikis, E.; Kivioja, J.; Marinelli, C.; Ryhanen, T.; Morpurgo, A.; et al. Science and Technology Roadmap for Graphene, Related Two-Dimensional Crystals, and Hybrid Systems. *Nanoscale* **2015**, *7*, 4598–4810.
- (4) Meng, Z.; Stolz, R. M.; Mendecki, L.; Mirica, K. A. Electrically-Transduced Chemical Sensors Based on Two-Dimensional Nanomaterials. *Chem. Rev.* **2019**, *119*, 478–598.
- (5) Celebi, K.; Buchheim, J.; Wyss, R. M.; Droudian, A.; Gasser, P.; Shorubalko, I.; Kye, J.-I.; Lee, C.; Park, H. G. Ultimate Permeation Across Atomically Thin Porous Graphene. *Science* **2014**, *344*, 289–292.
- (6) Jiang, L.; Fan, Z. Design of Advanced Porous Graphene Materials: From Graphene Nanomesh to 3D Architectures. *Nanoscale* **2014**, *6*, 1922–1945.
- (7) Moreno, C.; Vilas-Varela, M.; Kretz, B.; Garcia-Lekue, A.; Costache, M. V.; Paradinas, M.; Panighel, M.; Ceballos, G.; Valenzuela, S. O.; Peña, D.; Mugarza, A. Bottom-Up Synthesis of Multifunctional Nanoporous Graphene. *Science* **2018**, *360*, 199–203.
- (8) Georgakilas, V.; Tiwari, J. N.; Kemp, K. C.; Perman, J. A.; Bourlinos, A. B.; Kim, K. S.; Zboril, R. Noncovalent Functionalization of Graphene and Graphene Oxide for Energy Materials, Biosensing, Catalytic, and Biomedical Applications. *Chem. Rev.* **2016**, *116*, 5464–5519.
- (9) Woszczyna, M.; Winter, A.; Grothe, M.; Willunat, A.; Wundrack, S.; Stosch, R.; Weimann, T.; Ahlers, F.; Turchanin, A. All-Carbon Vertical van der Waals Heterostructures: Non-Destructive Functionalization of Graphene for Electronic Applications. *Adv. Mater.* **2014**, *26*, 4831–4837.
- (10) Hu, S.; Lozada-Hidalgo, M.; Wang, F. C.; Mishchenko, A.; Schedin, F.; Nair, R. R.; Hill, E. W.; Boukhvalov, D. W.; Katsnelson, M. I.; Dryfe, R. A. W.; Grigorieva, I. V.; Wu, H. A.; Geim, A. K. Proton Transport Through One-Atom-Thick Crystals. *Nature* **2014**, *516*, 227–230.
- (11) Emmrich, D.; Beyer, A.; Nadzeyka, A.; Bauerdick, S.; Meyer, J. C.; Kotakoski, J.; Götzhäuser, A. Nanopore Fabrication and Characterization by Helium Ion Microscopy. *Appl. Phys. Lett.* **2016**, *108*, 163103.
- (12) Koenig, S. P.; Wang, L.; Pellegrino, J.; Bunch, J. S. Selective Molecular Sieving Through Porous Graphene. *Nat. Nanotechnol.* **2012**, *7*, 728–732.
- (13) O’Hern, S. C.; Stewart, C. A.; Boutilier, M. S. H.; Idrobo, J.-C.; Bhaviripudi, S.; Das, S. K.; Kong, J.; Laoui, T.; Atieh, M.; Karnik, R. Selective Molecular Transport Through Intrinsic Defects in a Single Layer of CVD Graphene. *ACS Nano* **2012**, *6*, 10130–10138.
- (14) Georgakilas, V.; Otyepka, M.; Bourlinos, A. B.; Chandra, V.; Kim, N.; Kemp, K. C.; Hobza, P.; Zboril, R.; Kim, K. S. Functionalization of Graphene: Covalent and Non-Covalent Approaches, Derivatives and Applications. *Chem. Rev.* **2012**, *112*, 6156–6214.
- (15) Zhonghua, X.; Quanbin, D.; Jian-Feng, C.; Liming, D. Edge Functionalization of Graphene and Two-Dimensional Covalent Organic Polymers for Energy Conversion and Storage. *Adv. Mater.* **2016**, *28*, 6253–6261.
- (16) Yanbing, Y.; Xiangdong, Y.; Xuming, Z.; Shiting, W.; Da, W.; Anyuan, C.; Lei, L.; Quan, Y.; Xiangfeng, D. Ultrafine Graphene



Nanomesh with Large On/Off Ratio for High-Performance Flexible Biosensors. *Adv. Funct. Mater.* **2017**, *27*, 1604096.

(17) Kwon, S. S.; Yi, J.; Lee, W. W.; Shin, J. H.; Kim, S. H.; Cho, S. H.; Nam, S.; Park, W. I. Reversible and Irreversible Responses of Defect-Engineered Graphene-Based Electrolyte-Gated pH Sensors. *ACS Appl. Mater. Interfaces* **2016**, *8*, 834–839.

(18) Kwon, S. S.; Shin, J. H.; Choi, J.; Nam, S.; Park, W. I. Defect-Mediated Molecular Interaction and Charge Transfer in Graphene Mesh–Glucose Sensors. *ACS Appl. Mater. Interfaces* **2017**, *9*, 14216–14221.

(19) Eck, W.; Küller, A.; Grunze, M.; Völkel, B.; Götzhäuser, A. Freestanding Nanosheets from Crosslinked Biphenyl Self-Assembled Monolayers. *Adv. Mater.* **2005**, *17*, 2583–2587.

(20) Turchanin, A.; Götzhäuser, A. Carbon Nanomembranes. *Adv. Mater.* **2016**, *28*, 6075–6103.

(21) Turchanin, A.; Käfer, D.; El-Desawy, M.; Wöll, C.; Witte, G.; Götzhäuser, A. Molecular Mechanisms of Electron-Induced Cross-Linking in Aromatic SAMs. *Langmuir* **2009**, *25*, 7342–7352.

(22) Angelova, P.; Vieker, H.; Weber, N.-E.; Matei, D.; Reimer, O.; Meier, I.; Kurasch, S.; Biskupek, J.; Lorbach, D.; Wunderlich, K.; Chen, L.; Terfort, A.; Klapper, M.; Müllen, K.; Kaiser, U.; Götzhäuser, A.; Turchanin, A. A Universal Scheme to Convert Aromatic Molecular Monolayers into Functional Carbon Nanomembranes. *ACS Nano* **2013**, *7*, 6489–6497.

(23) Turchanin, A.; Beyer, A.; Nottbohm, C. T.; Zhang, X.; Stosch, R.; Sologubenko, A.; Mayer, J.; Hinze, P.; Weimann, T.; Götzhäuser, A. One Nanometer Thin Carbon Nanosheets with Tunable Conductivity and Stiffness. *Adv. Mater.* **2009**, *21*, 1233–1237.

(24) Zhang, X.; Neumann, C.; Angelova, P.; Beyer, A.; Götzhäuser, A. Tailoring the Mechanics of Ultrathin Carbon Nanomembranes by Molecular Design. *Langmuir* **2014**, *30*, 8221–8227.

(25) Penner, P.; Zhang, X.; Marschewski, E.; Behler, F.; Angelova, P.; Beyer, A.; Christoffers, J.; Götzhäuser, A. Charge Transport Through Carbon Nanomembranes. *J. Phys. Chem. C* **2014**, *118*, 21687–21694.

(26) Zhang, X.; Marschewski, E.; Penner, P.; Weimann, T.; Hinze, P.; Beyer, A.; Götzhäuser, A. Large-Area All-Carbon Nanocapacitors from Graphene and Carbon Nanomembranes. *ACS Nano* **2018**, *12*, 10301–10309.

(27) Yang, Y.; Dementyev, P.; Biere, N.; Emmrich, D.; Stohmann, P.; Korzetz, R.; Zhang, X.; Beyer, A.; Koch, S.; Anselmetti, D.; Götzhäuser, A. Rapid Water Permeation Through Carbon Nanomembranes with Sub-Nanometer Channels. *ACS Nano* **2018**, *12*, 4695–4701.

(28) Turchanin, A.; Weber, D.; Bünenfeld, M.; Kisielowski, C.; Fistul, M. V.; Efetov, K. B.; Weimann, T.; Stosch, R.; Mayer, J.; Götzhäuser, A. Conversion of Self-Assembled Monolayers into Nanocrystalline Graphene: Structure and Electric Transport. *ACS Nano* **2011**, *5*, 3896–3904.

(29) Matei, D. G.; Weber, N.-E.; Kurasch, S.; Wundrack, S.; Woszczyzna, M.; Grothe, M.; Weimann, T.; Ahlers, F.; Stosch, R.; Kaiser, U.; Turchanin, A. Functional Single-Layer Graphene Sheets from Aromatic Monolayers. *Adv. Mater.* **2013**, *25*, 4146–4151.

(30) Turchanin, A. Graphene Growth by Conversion of Aromatic Self-Assembled Monolayers. *Ann. Phys.* **2017**, *529*, 1700168.

(31) Mattoni, A.; Colombo, L. Crystallization Kinetics of Mixed Amorphous-Crystalline Nanosystems. *Phys. Rev. B: Condens. Matter Phys.* **2008**, *78*, 075408.

(32) Laibinis, P. E.; Whitesides, G. M.; Allara, D. L.; Tao, Y. T.; Parikh, A. N.; Nuzzo, R. G. Comparison of the Structures and Wetting Properties of Self-Assembled Monolayers of n-Alkanethiols on the Coinage Metal Surfaces, Copper, Silver, and Gold. *J. Am. Chem. Soc.* **1991**, *113*, 7152–7167.

(33) Jeong, H. M.; Lee, J. W.; Shin, W. H.; Choi, Y. J.; Shin, H. J.; Kang, J. K.; Choi, J. W. Nitrogen-Doped Graphene for High-Performance Ultracapacitors and the Importance of Nitrogen-Doped Sites at Basal Planes. *Nano Lett.* **2011**, *11*, 2472–2477.

(34) Kankate, L.; Turchanin, A.; Götzhäuser, A. On the Release of Hydrogen from the S–H Groups in the Formation of Self-Assembled Monolayers of Thiols. *Langmuir* **2009**, *25*, 10435–10438.

(35) Kankate, L.; Hamann, T.; Li, S.; Moskaleva, L. V.; Götzhäuser, A.; Turchanin, A.; Swiderek, P. Tracking Down the Origin of Peculiar Vibrational Spectra of Aromatic Self-Assembled Thiolate Monolayers. *Phys. Chem. Chem. Phys.* **2018**, *20*, 29918–29930.

(36) Jansen, R. J. J.; van Bekkum, H. XPS of Nitrogen-Containing Functional Groups on Activated Carbon. *Carbon* **1995**, *33*, 1021–1027.

(37) Onoue, M.; Han, M. R.; Ito, E.; Hara, M. Step-Wise Decomposition Process of Azobenzene Self-Assembled Monolayers. *Surf. Sci.* **2006**, *600*, 3999–4003.

(38) Zubavichus, Y.; Zhamikov, M.; Yang, Y.; Fuchs, O.; Umbach, E.; Heske, C.; Ulman, A.; Grunze, M. X-ray Photoelectron Spectroscopy and Near-Edge X-ray Absorption Fine Structure Study of Water Adsorption on Pyridine-Terminated Thiolate Self-Assembled Monolayers. *Langmuir* **2004**, *20*, 11022–11029.

(39) Thomas, A.; Fischer, A.; Goettmann, F.; Antonietti, M.; Muller, J.-O.; Schlogl, R.; Carlsson, J. M. Graphitic Carbon Nitride Materials: Variation of Structure and Morphology and Their Use as Metal-Free Catalysts. *J. Mater. Chem.* **2008**, *18*, 4893–4908.

(40) Wu, Z.-S.; Winter, A.; Chen, L.; Sun, Y.; Turchanin, A.; Feng, X.; Müllen, K. Three-Dimensional Nitrogen and Boron Co-doped Graphene for High-Performance All-Solid-State Supercapacitors. *Adv. Mater.* **2012**, *24*, 5130–5135.

(41) Sheng, Z.-H.; Shao, L.; Chen, J.-J.; Bao, W.-J.; Wang, F.-B.; Xia, X.-H. Catalyst-Free Synthesis of Nitrogen-Doped Graphene via Thermal Annealing Graphite Oxide with Melamine and Its Excellent Electrocatalysis. *ACS Nano* **2011**, *5*, 4350–4358.

(42) Casanovas, J.; Ricart, J. M.; Rubio, J.; Illas, F.; Jiménez-Mateos, J. M. Origin of the Large N 1s Binding Energy in X-ray Photoelectron Spectra of Calcined Carbonaceous Materials. *J. Am. Chem. Soc.* **1996**, *118*, 8071–8076.

(43) Matanovic, I.; Artyushkova, K.; Strand, M. B.; Dzara, M. J.; Pylypenko, S.; Atanassov, P. Core Level Shifts of Hydrogenated Pyridinic and Pyrrolic Nitrogen in the Nitrogen-Containing Graphene-Based Electrocatalysts: In-Plane vs Edge Defects. *J. Phys. Chem. C* **2016**, *120*, 29225–29232.

(44) Doniach, S.; Sunjic, M. Many-Electron Singularity in X-ray Photoemission and X-ray Line Spectra from Metals. *J. Phys. C: Solid State Phys.* **1970**, *3*, 285.

(45) Ferrari, A. C.; Basko, D. M. Raman Spectroscopy as a Versatile Tool for Studying the Properties of Graphene. *Nat. Nanotechnol.* **2013**, *8*, 235–246.

(46) Rasband, W. *ImageJ*, version 1.51; National Institutes of Health, USA. <https://imagej.nih.gov/ij/>, accessed January 31, 2017.

(47) Winter, A.; Ekinci, Y.; Götzhäuser, A.; Turchanin, A. Freestanding Carbon Nanomembranes and Graphene Monolayers Nanopatterned via EUV Interference Lithography. *2D Mater.* **2019**, *6*, 021002.

(48) Sarma, S. D.; Adam, S.; Hwang, E.; Rossi, E. Electronic Transport in Two-Dimensional Graphene. *Rev. Mod. Phys.* **2011**, *83*, 407.

(49) Jang, C.; Adam, S.; Chen, J. H.; Williams, E. D.; Das Sarma, S.; Fuhrer, M. S. Tuning the Effective Fine Structure Constant in Graphene: Opposing Effects of Dielectric Screening on Short- and Long-Range Potential Scattering. *Phys. Rev. Lett.* **2008**, *101*, 146805.

(50) Meric, I.; Han, M. Y.; Young, A. F.; Ozyilmaz, B.; Kim, P.; Shepard, K. L. Current Saturation in Zero-Bandgap, Topgated Graphene Field-Effect Transistors. *Nat. Nanotechnol.* **2008**, *3*, 654–659.

(51) Mueller, T.; Xia, F.; Freitag, M.; Tsang, J.; Avouris, P. Role of Contacts in Graphene Transistors: A Scanning Photocurrent Study. *Phys. Rev. B: Condens. Matter Mater. Phys.* **2009**, *79*, 245430.

(52) Efros, A. L.; Shklovskii, B. I. Critical Behaviour of Conductivity and Dielectric Constant near the Metal-Non-Metal Transition Threshold. *Phys. Status Solidi B* **1976**, *76*, 475–485.

- (53) Fournier, J.; Boiteux, G.; Seytre, G.; Marichy, G. Percolation Network of Polypyrrole in Conducting Polymer Composites. *Synth. Met.* **1997**, *84*, 839–840.
- (54) Alig, I.; Skipa, T.; Lellinger, D.; Bierdel, M.; Meyer, H. Dynamic Percolation of Carbon Nanotube Agglomerates in a Polymer Matrix: Comparison of Different Model Approaches. *Phys. Status Solidi B* **2008**, *245*, 2264–2267.
- (55) Shklovskii, B. I.; Efros, A. L. *Electronic Properties of Doped Semiconductors*; Springer Science & Business Media, 2013; Vol. 45.
- (56) Mattoni, A.; Colombo, L. Nonuniform Growth of Embedded Silicon Nanocrystals in an Amorphous Matrix. *Phys. Rev. Lett.* **2007**, *99*, 205501.
- (57) Winter, A.; George, A.; Neumann, C.; Tang, Z.; Mohn, M. J.; Biskupek, J.; Masurkar, N.; Reddy, A. L. M.; Weimann, T.; Hübner, U.; Kaiser, U.; Turchanin, A. Lateral Heterostructures of Two-Dimensional Materials by Electron-Beam Induced Stitching. *Carbon* **2018**, *128*, 106–116.